ROYAL SOCIETY OF CHEMISTRY

COMMUNICATION

Check for updates

Understanding the Ag–S interface stability and electrocatalytic activity of CO$_2$ electroreduction in atomically precise Ag$_{25}$ nanoclusters†

Yuting Ye,‡[a] Xia Zhou,‡[b] Yuping Chen,[a] Likai Wang [iD] *[b] and Qing Tang [iD] *[a]

Elucidating the catalytic properties of metal nanoclusters (NCs) with essentially the same structure but different core metals is of fundamental interest. Our current studies have demonstrated that the thiolated Ag$_{25}$(SR)$_{18}$ NC exhibits SR ligand leaching dynamics and electrocatalytic activity in CO$_2$ reduction distinct from those of its Au$_{25}$(SR)$_{18}$ NC structural analogue.

In recent years, small metal nanoclusters (NCs) made with atomic precision have attracted great attention in various fields such as catalysis, chemical sensing and bio-applications.[1–6] The use of atomically precise metal NCs could eliminate concerns of inhomogeneity, and their ultrasmall size (1–2 nm) minimizes the material gap between experiments and modelling, thus holding great promise in fundamental catalysis research.[7,8] In the large family of metal NCs protected by various ligands, the thiolate-protected metal NCs have attracted extensive research interest, wherein Au and Ag NCs are two extensively studied groups.[9–12] Thiolated Au NCs have been widely studied in many catalytic applications.[5,6,13,14] For example, gold NCs have been recognized for their exceptional electrocatalytic activities in electrocatalytic reduction of CO$_2$ to CO.[15] The effects of cluster size, shape, surface ligands and heterometal doping have been extensively employed to modulate the electrocatalytic activity and selectivity of gold NCs.[16–19]

Compared to the widely studied gold NCs, thiolated Ag NCs have been less extensively investigated, possibly due to their moderate stability, leading to a limited understanding of their catalytic properties,[20,21] In particular, there are few recent studies on Ag NCs for photocatalytic CO$_2$RR.[22,23] Investigating

Ag-based catalysts is of great importance for uncovering new catalytic mechanisms and utilizing metals that are less expensive than Au. Note that the catalytic properties of metal NCs are highly sensitive to the packing of atomic structures, and a subtle disturbance to the structure, composition and morphology may cause a significant change in the electronic and catalytic behaviors. In this regard, a direct comparison of catalytic performances of materials with essentially identical structures but distinct metal cores is of particular interest but has been hardly been pursued. In the large family of thiolate-protected metal NCs, the well-characterized Ag$_{25}$(SR)$_{18}$ provides an ideal model to study the effect of the core since this cluster and Au$_{25}$(SR)$_{18}$ share essentially the same structure. They both feature an icosahedral M$_{13}$ core protected by six V-shaped motifs arranged in a quasi-Th symmetry (Fig. S1, ESI†),[10] thus enabling a direct comparison of their catalytic activities.[10,24] Of note, recent studies have demonstrated that the Au–S interface in Au$_{25}$(SR)$_{18}$ NCs is unstable under electrochemical conditions, and would be attacked by water from electrolyte to lead to stripping of some of the thiolate ligands and hence expose under-coordinated Au atoms to the surface.[5,25,26] Since the Ag–S bond is expected to be stronger and more ionic than the Au–S bond based on the difference in electronegativity between S and these two metals, it would be interesting to determine whether the Ag–S interface would become destabilized under electrochemical environments. If the thiolate ligands in Ag$_{25}$(SR)$_{18}$ can be eliminated from the Ag–S interface, then it would be of great importance to investigate the electrocatalytic response of the exposed Ag sites in comparison to Au in the dethiolated Au$_{25}$ counterpart.

Therefore, to gain a better understanding of the catalytic mechanism of Ag NCs, we selected Ag$_{25}$(SR)$_{18}$ as our research model, and first performed density functional theory (DFT) calculations to investigate its dynamic stability in electrochemical conditions.[27–30] To reduce the computational cost, the SR ligands were simplified to be –SCH$_3$.[5] The computational details are provided in ESI.† To simulate the cluster/water interface, Ag$_{25}$ and Au$_{25}$ were placed in respective periodic

[a] School of Chemistry and Chemical Engineering, Chongqing Key Laboratory of Chemical Theory and Mechanism, Chongqing University, Chongqing 401331, China. E-mail: qingtang@cqu.edu.cn

[b] School of Chemistry and Chemical Engineering, Shandong University of Technology, Zibo, Shandong, 255049, China. E-mail: lkwangchem@sdut.edu.cn

‡ These two authors contributed equally to this work.

boxes, each with dimensions of $20 \times 20 \times 30$ Å^3 and surrounded by 90 explicit water molecules with a density of about 1 g cm^{-3} (Fig. S2, ESI†). The potential of the entire system was regulated by introducing different amounts of Na atoms into the aqueous layer while the overall system was kept charge neutral. In this way, $U_{RHE} = (\Phi - 4.44)/e + 0.0592 \times$ pH would give a different applied potential U depending on the value of the work function (Φ) for each model.[31] Under a neutral pH condition (pH = 7), the addition of 1, 2 and 3 Na atoms into the Ag$_{25}$/water system would thus yield potentials of, respectively, 0.33 V, −0.84 V and −1.10 V vs. reversible hydrogen electrode (RHE).

According to the previous studies,[5,26] the desorption of thiolate ligands from the Au$_{25}$(SR)$_{18}$ surface is promoted by H$_2$O attacking the S atom to initiate the weakening and breakage of Au–S bonds. In the case of Ag$_{25}$(SCH$_3$)$_{18}$ NCs, the –SR ligand would be expected to undergo a similar leaching process, and the corresponding control variable (CV) for H adsorption (step 1) and Ag–S breakage (step 2) are defined schematically in Fig. S3 (ESI†). Our constrained *ab initio* molecular dynamics (AIMD) simulations at 300 K indicated the dynamic behavior of the Ag–S interface to be strongly dependent on the applied potential (Fig. 1a). At a positive potential of 0.33 V (Fig. S4, ESI†), the Ag–S interface is very stable: an attack of water from the solution onto the ligated S atom to form an adsorbed S–H bond and solvated OH$^-$ species would have to overcome a very high barrier of 1.28 eV. For the potential shifted negatively to −0.84 V, the barrier for the water attack forming an S–H bond decreases to 1.04 eV (Fig. 1b). Note that the water molecule prefers to attack the

S atom from the exterior thiolate ligand initially coordinated to two staple Ag atoms (Fig. 1a). This picture is quite different from that for the previously reported Au$_{25}$(SR)$_{18}$ NC,[5] where the water molecule tends to attack the interior thiolate ligand initially coordinated to one staple Au and one icosahedral surface Au. Formation of the S–H bond is accompanied by a weakening of and hence more easily breakable Ag–S bond (Fig. 1c). Note that at U_{RHE} = −0.84 V, only one staple Ag–S bond is broken with a small free energy barrier of 0.16 eV, while the other staple Ag still strongly interacts with the coordinated S atom (Fig. 1a). For the potential further decreased to U_{RHE} = −1.10 V, one of the staple Ag–S bonds first breaks spontaneously after the structural relaxation at 0.8 ps, followed by formation of an S–H bond with a moderate barrier of 0.67 eV, and the other staple Ag–S bond can be easily broken with a negligibly small barrier of 0.08 eV, which ultimately results in the complete removal of the –SCH$_3$ ligand, forming a free HSCH$_3$ molecule dissolved in solution and exposing two dethiolated Ag sites (exposed Ag–Ag bond length of 2.74 Å). These simulations indicated that the applied potential can significantly affect the leaching dynamics of the Ag–S interface, and a lower reduction potential could kinetically promote the removal of thiolate ligands.

As a comparison, we also performed AIMD simulations on the Au$_{25}$(SCH$_3$)$_{18}$ analogue in the same neutral environment. In this case, additions of one and two Na atoms into the water layer correspond to applied potential U_{RHE} values of 0.11 V and −0.60 V, respectively. Note that addition of 3 Na atoms would lead to severe deformation of the Au$_{25}$ NC due to an especially low potential produced (U_{RHE} = −1.30 V, Fig. S5, ESI†), which is beyond our consideration. Similar to the case in Ag$_{25}$, the ligand leaching in Au$_{25}$ was also found to be dependent on potential. At U_{RHE} = 0.11 V, adsorption of water-dissociation-derived H onto the S atom from the interior thiolate ligand has to overcome a high barrier of 1.13 eV (Fig. S6, ESI†). For the potential lowered to −0.60 V (Fig. 2), the attack of S by water becomes much more facile, and the formation of the S–H bond
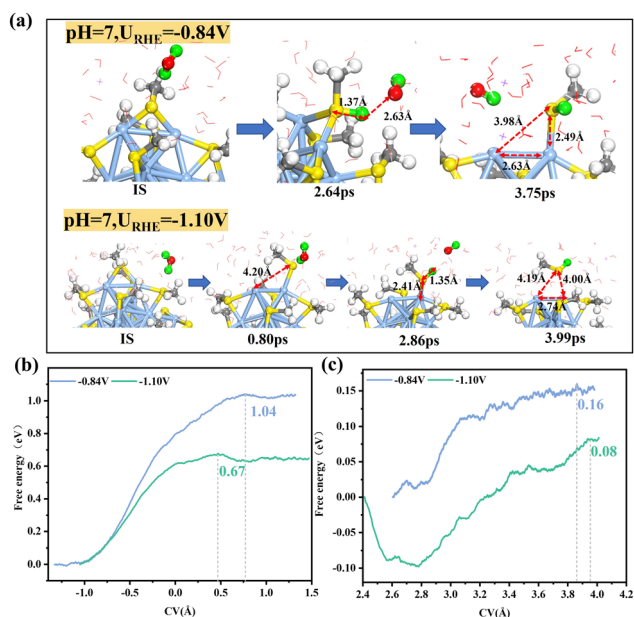

Fig. 1 (a) Schematic of local structures formed during adsorption of *H onto the S site and during Ag–S bond breaking in Ag$_{25}$(SR)$_{18}$ at U_{RHE} = −0.84 V and −1.10 V. (b) Integral free energy curves for *H adsorption and (c) Ag–S bond breaking at U_{RHE} = −0.84 V and −1.10 V, respectively. The Ag, S, C, O and H atoms are shown as pale blue, yellow, grey, red and white spheres, respectively. The H from the attacking H$_2$O is colored in green.
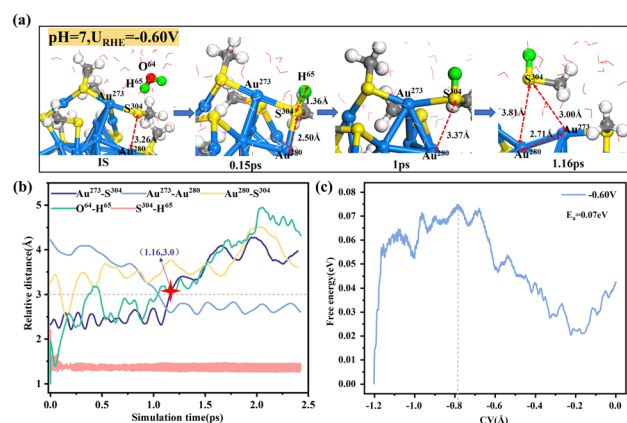

Fig. 2 (a) Schematic of the local structures formed during *H adsorption and Au–S breaking in Au$_{25}$(SCH$_3$)$_{18}$ at U_{RHE} = −0.60 V. (b) Statistics of the relative distances between representative atoms and (c) the integral free energy curve during constrained DFT-MD simulations at U_{RHE} = −0.60 V.

is accompanied by the consecutive breaking of the surface Au–S bond and the staple Au–S bond. Note the difference between the water attack site in Au_{25} (interior thiolate) and that in Ag_{25} (exterior thiolate). To understand this difference, we analysed the charge states of the two possible S sites. The Bader charge analysis carried out (Fig. S7, ESI†) revealed that in Ag_{25}, the exterior S site carries a more negative charge of $-0.37|e|$ as compared to the interior S site ($-0.35|e|$); conversely, in Au_{25}, the analysis indicated the interior S to be more negatively charged ($-0.30|e|$) than the exterior S site ($-0.12|e|$). The S site bearing a more negative charge is prone to be attacked by H_2O and is hence more reactive. At 1.16 ps, the two breaking Au–S bonds reach an equilibrium length of greater than 3 Å, at which point the $–SCH_3$ ligand can be considered to be completely removed, and the two exposed Au atoms are bonded to each other with a shortened bond length of 2.71 Å. In particular, the negligible barrier of 0.07 eV (Fig. 2c) indicates that the thiolate leaching in Au_{25} occurs spontaneously at a negative reduction potential. Notably, at a comparable reduction potential (-0.84 V in Ag_{25} *vs.* -0.60 V in Au_{25}), the leaching of thiolate from the Ag–S interface is kinetically more difficult than that from the Au–S interface, which is closely related to the difference between their M–S bond strengths.

After the removal of –SR ligands, the dethiolated metal atoms can serve as the catalytically active sites. Our Bader charge analysis (Table S1, ESI†) revealed that the exposed two Ag atoms are positively charged ($0.06|e|$ and $0.03|e|$), while the exposed two Au atoms are negatively charged ($-0.09|e|$ and $-0.13|e|$), with this difference between the exposed Ag and Au atoms implying that their catalytic properties could be different. We thus proceeded to investigate the dethiolated Ag_{25} and Au_{25} in the electrocatalytic CO_2 reduction reaction (CO_2RR). Fig. 3 shows the calculated integral free energy curves of the four elementary reaction steps for Ag_{25} and Au_{25} under the

same neutral condition with two Na atoms added into the water layer. As shown in Fig. 3a, the CO_2 reactant can be effectively captured and activated at the exposed metal sites with very low kinetic barriers (0.22 eV in Ag_{25} and 0.13 eV in Au_{25}). In Ag_{25}, the CO_2 is bonded to two staple Ag atoms in a bridging manner, while in Au_{25}, it is only singly bonded to the staple Au atom. After the activation step, the nearest water molecule would approach $*CO_2$ to form $*COOH$ and a solvated OH^- species (Fig. 3b). This step has to overcome a relatively high barrier of about 0.93 eV in Ag_{25}, as compared to 0.71 eV in Au_{25}. Subsequently, the approach of another H_2O molecule to the O atom at the O–H end of $*COOH$ leads to formation of adsorbed $*CO$ and H_2O (Fig. 3c). This step needs to overcome a high barrier of 0.81 eV in Au_{25}, while in Ag_{25}, the barrier is only 0.68 eV. The final step corresponds to $*CO$ desorption, forming CO gas and exposing the reactive metal sites (Fig. 3d). This step is very facile, and the desorption barrier is very low, about 0.23 eV in Ag_{25} and 0.28 eV in Au_{25}. The above analysis indicated a different rate-determining step (RDS) of the CO_2RR for Ag_{25} than for Au_{25}. In Ag_{25}, the highest potential barrier corresponds to the formation of $*COOH$, whereas in Au_{25}, the most difficult step is the formation of $*CO$. This analysis has thus demonstrated that changing the metal to another one with sufficiently different properties can change the RDS. We also examined the distributions of water density and hydrogen bonds at the cluster/water interface during the CO_2RR for Au_{25} and Ag_{25} (Fig. S8, ESI†). The results showed slightly denser water density at the Au_{25}/water interface, accompanied by more hydrogen bonds in Au_{25} than in Ag_{25}. This observation suggested more water molecules to be accessible around the electrochemical interface of the Au_{25} NC, thus facilitating the reaction kinetics for water and proton transfer during the CO_2RR.

Furthermore, to probe the CO_2RR selectivity, we also investigated its competitive hydrogen evolution reaction (HER). In the first Volmer step (Fig. S9a, ESI†), the dissociation of H_2O to form an $*H$ intermediate requires a high barrier, of 1.45 eV in Ag_{25} and 1.07 eV in Au_{25}, to be overcome. In the subsequent Heyrovsky step, the adsorbed $*H$ would then combine with another H from water to produce H_2 and a solvated OH^- species. This step has to overcome a high barrier of 1.34 eV in Au_{25} and 1.27 eV in Ag_{25} (Fig. S9b, ESI†). Such a high barrier effectively inhibits HER at the exposed metal sites, thus ensuring the high selectivity of electroreduction of CO_2 to CO in both Ag_{25} and Au_{25}.

To further probe whether ligand simplification would affect the reaction kinetics, we replaced the simplified $–SCH_3$ near the exposed metal site with the longer $–SC_6H_{13}$ ligand and calculated the corresponding free energy barriers of the CO_2RR (Fig. S10, ESI†) and HER (Fig. S11, ESI†). In contrast to the simplified $–SCH_3$, the long-chain $–SC_6H_{13}$ ligand facilitates CO_2 activation and $*CO$ formation in Ag_{25} as well as $*COOH$ formation in Au_{25}. However, upon replacing the ligand, the energy barrier for the RDS ($*COOH$ formation in Ag_{25} and $*CO$ formation in Au_{25}) remains almost unchanged for both NCs. In the HER process, the presence of the long-chain $–SC_6H_{13}$ greatly decreases the barrier for the Volmer and Heyrovsky steps, yet the barrier for the RDS is still higher than that in
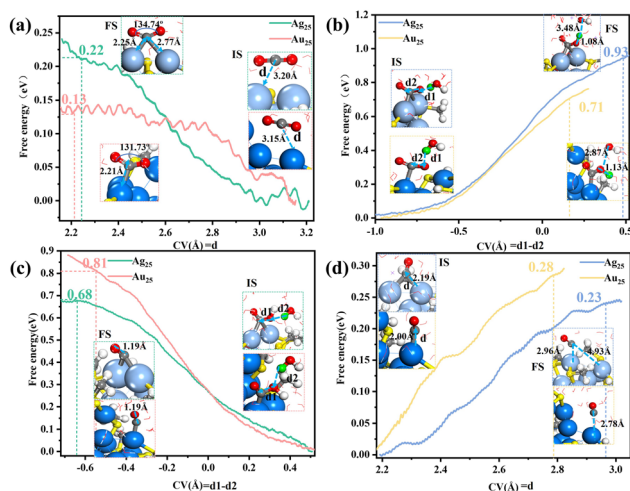

Fig. 3 Comparison of the integral free energy curves between Ag_{25} and Au_{25} in (a) CO_2 activation, (b) $*COOH$ formation, (c) $*CO$ formation and (d) CO desorption as determined from constrained AIMD simulations. The local structures of the initial state (IS), final state (FS) and the defined collective variable (CV, $d_1 - d_2$ or d) are shown in the insets.
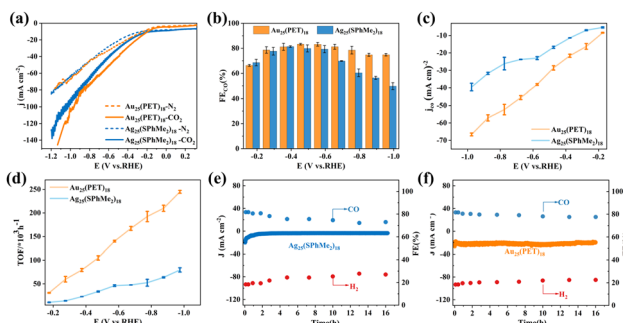
Fig. 4 Electrocatalytic CO$_2$RR performance in a CO$_2$ flow cell with 1 M KOH electrolyte. (a) LSV curves of Ag$_{25}$(SphMe$_2$)$_{18}$ and of Au$_{25}$(PET)$_{18}$, each in N$_2$-saturated or CO$_2$-saturated 1 M KOH electrolyte. (b) Faradaic efficiency of CO (FE$_{CO}$), (c) fractional current density of CO (j_{CO}), and (d) turnover frequency (TOF) of CO for Ag$_{25}$ and Au$_{25}$ at indicated potentials. (e) and (f) Tests of long-term stability of (e) Ag$_{25}$ and (f) Au$_{25}$ in the CO$_2$RR at −0.38 V.

the CO$_2$RR, suggesting the higher selectivity for CO$_2$ electroreduction. These results indicated that the predicted reaction kinetics and selectivity based on the simplified –SCH$_3$ should be qualitatively reliable.

Furthermore, we conducted experiments to verify the prediction. As shown in Fig. S12 (ESI†), the Ag$_{25}$(SphMe$_2$)$_{18}$ NC (SphMe$_2$ = 2,4-dimethylbenzenethiol) sample exhibits characteristic absorption peaks at 390 nm, 490 nm, and 675 nm, while Au$_{25}$(PET)$_{18}$ (PET = phenylethylmercaptan) NC sample exhibits characteristic absorption peaks at 400 nm, 450 nm, and 670 nm, consistent with those reported in the literature.[24,32] Their performance in the CO$_2$RR was first evaluated by performing linear sweep voltammetry (LSV). As shown in Fig. 4a, the current density for each of the NCs is larger in CO$_2$-saturated electrolyte than in N$_2$-saturated electrolyte, suggesting greater involvement of current in the CO$_2$RR to CO. The CO faradaic efficiency (FE$_{CO}$) measurements (Fig. 4b) showed Au$_{25}$(PET)$_{18}$ achieving an FE$_{CO}$ higher than that of Ag$_{25}$(SphMe$_2$)$_{18}$. The current density (j_{CO}) of Au$_{25}$(PET)$_{18}$ is also higher than that of Ag$_{25}$(SphMe$_2$)$_{18}$ (Fig. 4c). Moreover, from Fig. 4d, it is evident that the turnover frequency (TOF) value for Au$_{25}$(PET)$_{18}$ NCs is greater than that of Ag$_{25}$(SphMe$_2$)$_{18}$. These measurements suggested a better intrinsic activity and higher catalytic rate for Au$_{25}$(PET)$_{18}$ than for Ag$_{25}$(SphMe$_2$)$_{18}$. Additionally, the stability tests (Fig. 4e and f) indicated better FE$_{CO}$ stability and current density stability demonstrated by Au$_{25}$(PET)$_{18}$ during continuous operation at −0.38 V for 16 hours. Evidently, these results agreed well with the theoretical predictions, where the inferior performance of Ag$_{25}$ could be correlated to its poorer ligand etching kinetics and higher RDS barrier in the CO$_2$RR process.

In summary, our studies have demonstrated distinct interface dynamics and the CO$_2$RR mechanisms for Au$_{25}$ and Ag$_{25}$, which would be expected to inspire the development of functional nanostructures with enhanced catalytic properties through metal core engineering.

Data availability

The data supporting this article have been included as part of the ESI.†

Conflicts of interest

There are no conflicts to declare.

Notes and references

1 S. Chen, S. Wang, J. Zhong, Y. Song, J. Zhang, H. Sheng, Y. Pei and M. Zhu, *Angew. Chem., Int. Ed.*, 2015, **127**, 3188–3192.
2 Z. Chen, A. G. Walsh, X. Wei, M. Zhu and P. Zhang, *J. Phys. Chem. C*, 2022, **126**, 12721–12727.
3 Y. Du, H. Sheng, D. Astruc and M. Zhu, *Chem. Rev.*, 2019, **120**, 526–622.
4 J. H. Lee, S. Kattel, Z. Xie, B. M. Tackett, J. Wang, C. J. Liu and J. G. Chen, *Adv. Funct. Mater.*, 2018, **28**, 1804762.
5 F. Sun, L. Qin, Z. Tang, G. Deng, M. S. Bootharaju, Z. Wei, Q. Tang and T. Hyeon, *Chem. Sci.*, 2023, **14**, 10532–10546.
6 Q. Yao, Z. Wu, Z. Liu, Y. Lin, X. Yuan and J. Xie, *Chem. Sci.*, 2021, **12**, 99–127.
7 R. Jin, G. Li, S. Sharma, Y. Li and X. Du, *Chem. Rev.*, 2020, **121**, 567–648.
8 S. Li, A. V. Nagarajan, Y. Li, D. R. Kauffman, G. Mpourmpakis and R. Jin, *Nanoscale*, 2021, **13**, 2333–2337.
9 M. Hesari and Z. Ding, *Acc. Chem. Res.*, 2017, **50**, 218–230.
10 C. P. Joshi, M. S. Bootharaju, M. J. Alhilaly and O. M. Bakr, *J. Am. Chem. Soc.*, 2015, **137**, 11578–11581.
11 C. Liu, T. Li, H. Abroshan, Z. Li, C. Zhang, H. J. Kim, G. Li and R. Jin, *Nat. Commun.*, 2018, **9**, 744.
12 X. Zhu, L. Chen, Y. Liu and Z. Tang, *POM*, 2023, **2**, 9140031.
13 P. Zhang, *J. Phys. Chem. C*, 2014, **118**, 25291–25299.
14 F. Sun, C. Deng, S. Tian and Q. Tang, *ACS Catal.*, 2021, **11**, 7957–7969.
15 D. R. Kauffman, D. Alfonso, C. Matranga, H. Qian and R. Jin, *J. Am. Chem. Soc.*, 2012, **134**, 10237–10243.
16 S. Li, A. V. Nagarajan, D. R. Alfonso, M. Sun, D. R. Kauffman, G. Mpourmpakis and R. Jin, *Angew. Chem., Int. Ed.*, 2021, **60**, 6351–6356.
17 S. Li, D. Alfonso, A. V. Nagarajan, S. D. House, J. C. Yang, D. R. Kauffman, G. Mpourmpakis and R. Jin, *ACS Catal.*, 2020, **10**, 12011–12016.
18 X. Liu, E. Wang, M. Zhou, Y. Wan, Y. Zhang, H. Liu, Y. Zhao, J. Li, Y. Gao and Y. Zhu, *Angew. Chem., Int. Ed.*, 2022, **134**, e202207685.
19 J. Wang, F. Xu, Z. Y. Wang, S. Q. Zang and T. C. Mak, *Angew. Chem., Int. Ed.*, 2022, **61**, e202207492.
20 R. Jin, S. Zhao, Y. Xing and R. Jin, *CrystEngComm*, 2016, **18**, 3996–4005.
21 S. Yoo, S. Yoo, G. Deng, F. Sun, K. Lee, H. Jang, C. W. Lee, X. Liu, J. Jang, Q. Tang, Y. J. Hwang, T. Hyeon and M. S. Bootharaju, *Adv. Mater.*, 2024, **36**, 2313032.
22 Y. Feng, F. Fu, L. Zeng, M. Zhao, X. Xin, J. Liang, M. Zhou, X. Fang, H. Lv and G. Y. Yang, *Angew. Chem., Int. Ed.*, 2024, **63**, e202317341.
23 Y. Xiong, H. Chen, Y. Hu, S. Yang, X. Xue, L. He, X. Liu, J. Ma and Z. Jin, *Nano Lett.*, 2021, **21**, 8693–8700.
24 M. Zhu, W. T. Eckenhoff, T. Pintauer and R. Jin, *J. Phys. Chem. C*, 2008, **112**, 14221–14224.
25 H. Seong, V. Efremov, G. Park, H. Kim, J. S. Yoo and D. Lee, *Angew. Chem., Int. Ed.*, 2021, **133**, 14684–14691.
26 F. Sun, L. Qin, Z. Tang and Q. Tang, *Chem. Sci.*, 2024, **15**, 16142–16155.
27 H. Cao, Z. Zhang, J.-W. Chen and Y.-G. Wang, *ACS Catal.*, 2022, **12**, 6606–6617.
28 I. V. Chernyshova and S. Ponnurangam, *Phys. Chem. Chem. Phys.*, 2019, **21**, 8797–8807.
29 J. A. Gauthier, M. Fields, M. Bajdich, L. D. Chen, R. B. Sandberg, K. Chan and J. K. Nørskov, *J. Phys. Chem. C*, 2019, **123**, 29278–29283.
30 S. Li, A. V. Nagarajan, X. Du, Y. Li, Z. Liu, D. R. Kauffman, G. Mpourmpakis and R. Jin, *Angew. Chem., Int. Ed.*, 2022, **134**, e202211771.
31 K. Xie, F. Wang, F. Wei, J. Zhao and S. Lin, *J. Phys. Chem. C*, 2022, **126**, 5180–5188.
32 X. Liu, J. Yuan, C. Yao, J. Chen, L. Li, X. Bao, J. Yang and Z. Wu, *J. Phys. Chem. C*, 2017, **121**, 13848–13853.